ACS APPLIED MATERIALS & INTERFACES

Research Article

www.acsami.org

Nanoscopy of Phase Separation in $In_xGa_{1-x}N$ Alloys

Yohannes Abate,*[†,‡] Daniel Seidlitz,[†,‡] Alireza Fali,[†,‡] Sampath Gamage,[†,‡] Viktoriia Babicheva,[†,‡] Vladislav S. Yakovlev,[†,‡] Mark I. Stockman,[†,‡] Ramon Collazo,[§] Dorian Alden,[§] and Nikolaus Dietz[†,‡]

[†]Department of Physics and Astronomy, Georgia State University, Atlanta, Georgia 30303, United States

[‡]Center for Nano-Optics (CeNO), Georgia State University, Atlanta, Georgia 30303, United States

[§]Material Science and Engineering, North Carolina State University, Raleigh, North Carolina 27695, United States

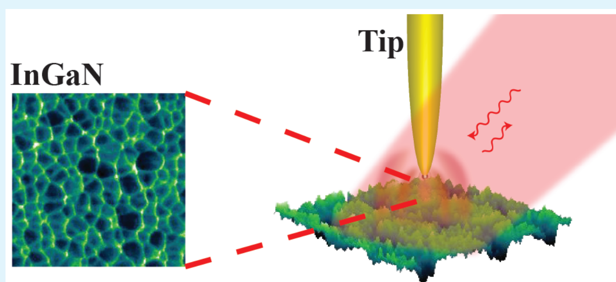

ABSTRACT: Phase separations in ternary/multinary semiconductor alloys is a major challenge that limits optical and electronic internal device efficiency. We have found ubiquitous local phase separation in $In_{1-x}Ga_xN$ alloys that persists to nanoscale spatial extent by employing high-resolution nanoimaging technique. We lithographically patterned InN/sapphire substrates with nanolayers of $In_{1-x}Ga_xN$ down to few atomic layers thick that enabled us to calibrate the near-field infrared response of the semiconductor nanolayers as a function of composition and thickness. We also developed an advanced theoretical approach that considers the full geometry of the probe tip and all the sample and substrate layers. Combining experiment and theory, we identified and quantified phase separation in epitaxially grown individual nanoalloys. We found that the scale of the phase separation varies widely from particle to particle ranging from all Ga- to all In-rich regions and covering everything in between. We have found that between 20 and 25% of particles show some level of Ga-rich phase separation over the entire sample region, which is in qualitative agreement with the known phase diagram of $In_{1-x}Ga_xN$ system.

KEYWORDS: *indium gallium nitride alloys, phase separation semiconductors, composition profile, nanospectroscopy, near-field*

■ INTRODUCTION

Ternary $In_{1-x}Ga_xN$ alloys are at the heart of modern technological application, such as light emitting diodes (LEDs) and laser diodes (LDs).[1−6] Although tremendous progress has been made in the capacity to tune the bandgap of these materials, fabrication of nanostructures that exhibit desired optoelectronic properties is still extremely challenging. This is partly due to a lack of effective methods to realize the formation of homogeneous multiquantum wells (MQWs) and/or quantum dots (QDs) with desirable composition profiles. Better understanding of phase purity/separation within QDs and better control of the nanoscale composition profiles and, hence, the materials properties will allow for the design of these alloys in complex structures for targeted device applications.[7−10] Investigation of nanoscale phase profiles of semiconductors naturally requires probing techniques that combine high spatial resolution and chemical identification simultaneously.[4,7−9,11−17,31]

Phase separation is a general phenomenon that exists in many compound semiconductor materials having vastly different partial pressures or large lattice mismatch.[7−10,16] Because of the complex interplay of strain, miscibility and thermodynamic effects between the substrate and different materials, the atoms segregate to form nonuniform distributions of mixed alloys. Phase separation results in alloys with statistically distributed compositions and modifies bandgap properties that ultimately determine the optoelectronic performances of semiconductor devices. Although transmission electron microscopy (TEM) offers atomic spatial resolution, quantitative analysis of image contrast is challenging due to dynamic electron scattering variations for thin samples.[18] Optical spectroscopy techniques such as photoluminescence (PL) and Fourier transform infrared spectroscopy (FTIR) are commonly used to analyze composition profiles in semiconductors and to correlate phase separation with various growth methods.[10,17,19−21] However, these techniques cannot be applied to study phase separation on individual nanostructures and QDs (5−100 nm range) owing to the extremely small IR absorption cross sections and the diffraction-limited spatial resolution. By contrast, scattering-type scanning near-field infrared nanoscopy (s-SNIN) offers spatial resolution several orders of magnitude below the diffraction limit. Resolution is only determined by the apex radius of the probe tip and not by the wavelength of light.[22] In s-SNIN the sharp metallic probe tip serves as an IR antenna channeling the incident radiation into a nanolocalized and enhanced near-field at its apex. The local near-field interaction between the probe tip and the sample modifies the tip-scattered radiation depending on the optical properties of the sample. The backscattered signal is detected in the far field via an interferometric detection scheme

Received: June 6, 2016
Accepted: August 17, 2016
Published: August 17, 2016

© 2016 American Chemical Society

DOI: 10.1021/acsami.6b06766
ACS Appl. Mater. Interfaces 2016, 8, 23160−23166

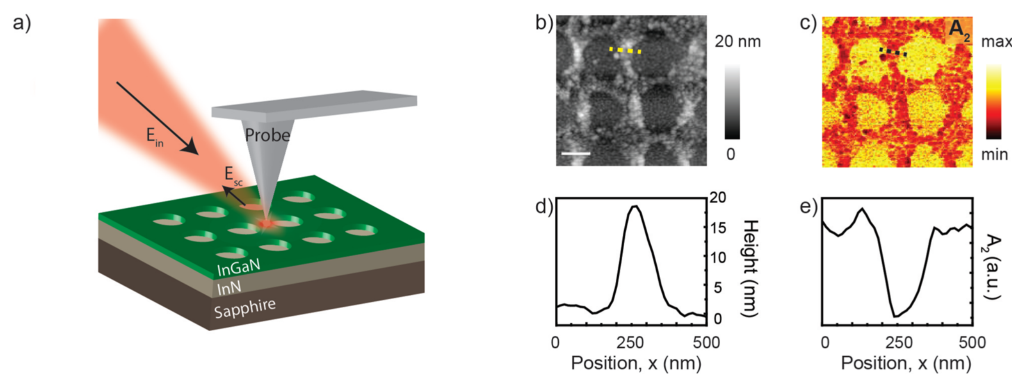

Figure 1. s-SNIN experimental setup and imaging. (a) Schematics of the s-SNIN setup. An oscillating probe tip, illuminated by a focused IR laser images InGaN nanostructures. (b) The topography and (c) the second-harmonic near-field amplitude (A_2) of a lithographically patterned $In_{1-x}Ga_xN$ nanolayer on a InN substrate. (d) Topographic and (e) A_2 line profiles showing higher islands having a lower A_2 contrast.

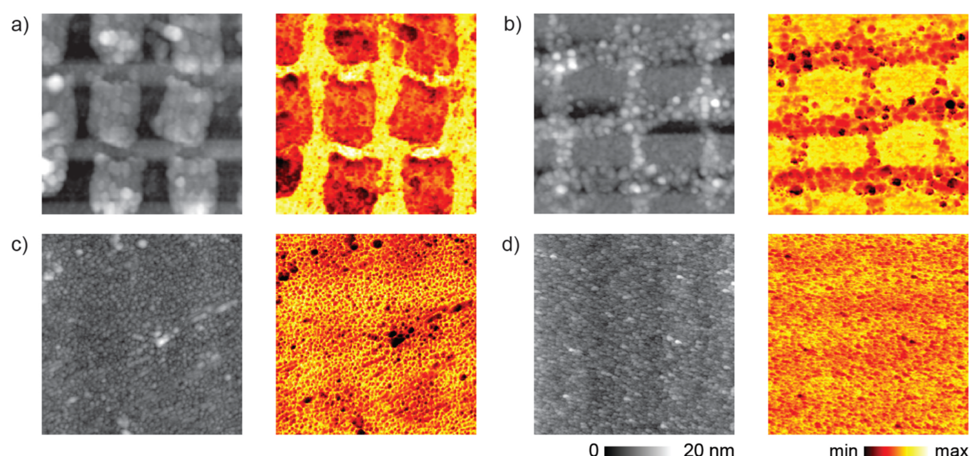

Figure 2. s-SNIN images of patterned nanolayers. (a) Topography and IR amplitude images of 20 nm-thick $In_{0.8}Ga_{0.2}N$. (b) Topography and IR amplitude images of 9 nm-thick $In_{0.5}Ga_{0.5}N$. (c) Topography and IR amplitude images of 1.5 nm-thick GaN. (d) Topography and IR amplitude images of 2.4 nm-thick Ga.

and provides nanoscale-resolved IR near-field images enabling local chemical composition profiling of the sample.[23,24] Elucidation of the experimental IR near-field images depends on theoretical modeling which still is a challenging undertaking. A realistic simulation must take into account the near-field interaction between the whole conical geometry of the probe tip, the complex sample structure and the substrate layers for a reliable interpretation of experimental data.

In this work, we have found local phase separation in $In_{1-x}Ga_xN$ alloys at nanometer spatial scale using high-resolution s-SNIN technique in the mid-IR spectral region. Via a combination of CVD and photolithography we patterned nanolayers with thickness down to a few atomic layers. These controlled samples allowed us to quantify the near-field infrared response of $In_{1-x}Ga_xN$ nanostructures. We first calibrated the near-field IR amplitude contrast as a function of composition and thickness of the semiconductor nanolayers. We then used this quantitative lead to identify phase separation in individual QDs. A novel theoretical model based on the finite-elements method (FEM) was developed to guide the experiments. Unlike previous models that consider the probe conical tip as approximate point dipoles[25] or spheroids, our model considers the full geometry of the tip, as well as all the sample and substrate layers.

RESULTS AND DISCUSSION

Figure 1a shows schematic of the s-SNIN experimental setup. An AFM tip coated with PtIr, oscillating at a resonance frequency of $f \approx 280$ kHz is irradiated with a focused quantum cascade laser (QCLs) at 45° with respect to the sample surface (Figure 1a). The scattered signal from the tip−sample interface region is demodulated at harmonics of the tip resonance frequency (nf, $n > 1$) and detected by phase-modulation (pseudoheterodyne) interferometry, producing simultaneous topography and optical images. Figure 1b and c show the topography and third-harmonic near-field amplitude optical images (A_3) of a MEPA-MOCVD-grown lithographically patterned InGaN sample on InN substrate (see Methods). The topographic image and the accompanying line profile (Figure 1d) show a height of ∼18 nm of InGaN. The near-field IR contrast in Figure 1c is related to the modification of the backscattered IR light (λ = 10.5 μm) via the near-field interaction of the probing tip and sample. One can see a distinct bright contrast for topographically lower structures and a dark contrast for topographically higher structures as shown in the images and line profiles in Figure 1b−e. As well-known, the backscattered IR signal offers a map of the dielectric constant (ε) of the sample, where a higher amplitude contrast corresponds to a larger value of $Re(\varepsilon)$.[23,26,27] On the basis of lithographical preparation, topographically higher structures (Figure 1b and d) are made up of InGaN whereas the

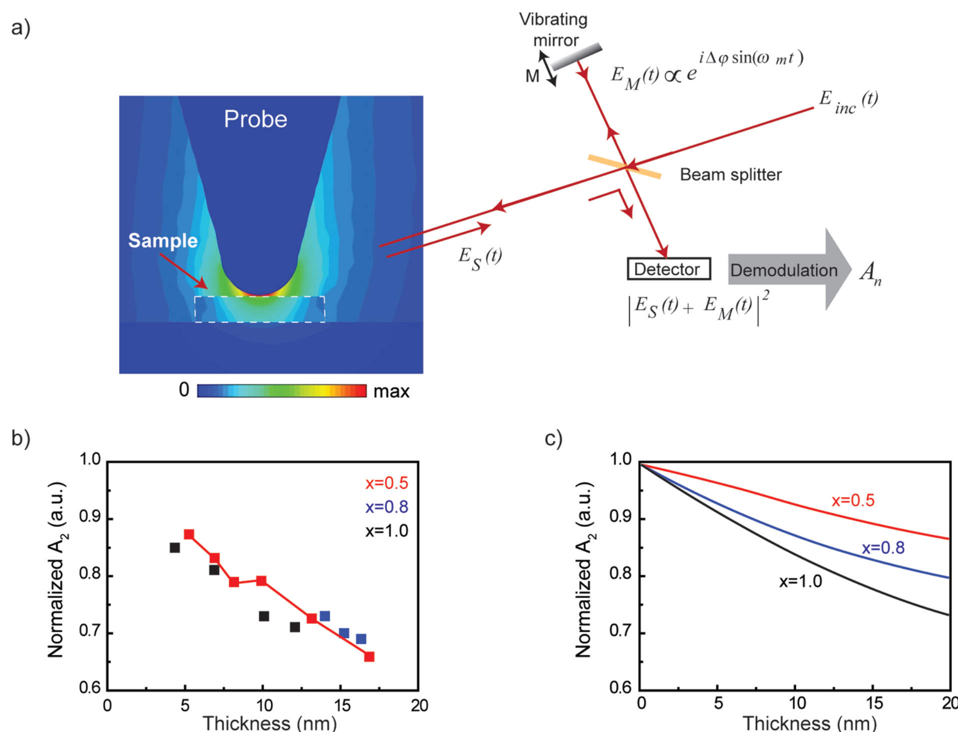

Figure 3. Theoretical and experimental description and characteristics $In_{1-x}Ga_xN$ samples. (a) Schematic illustration of the advanced FEM-based s-SNIN theoretical model used to calculate the near-field interaction of probe and sample. (b) A plot of the normalized experimental and (c) theoretical s-SNIN amplitude signal as a function of the thickness and composition of $In_{1-x}Ga_xN$ alloys.

underlying substrate pattern is InN. A comparison of the topography and s-SNIN IR images suggests that $Re(\varepsilon)$ is larger for InN than for InGaN (Figure 1c and e) at the laser wavelength, λ = 10.5 μm, used for these experiments. In this way, it is possible to quantify the permittivity of $In_{1-x}Ga_xN$ nanolayers, with respect to the InN substrate, depending on their chemical composition and thickness. For this purpose, we prepared several patterned samples with various $In_{1-x}Ga_xN$ compositions and thickness ranging from subtens of nanometers down to few-monolayer 2D structures on the InN/sapphire substrate. Figure 2 shows topography and IR amplitude images for four different compositions and thicknesses: $In_{0.8}Ga_{0.2}N$, thickness 20 nm (Figure 2a), $In_{0.5}Ga_{0.5}N$, thickness 9 nm (Figure 2b), GaN, thickness 1.5 nm (Figure 2c), and Ga, thickness 2.4 nm (Figure 2d). Although AFM topographic mapping indicates the height differences between the two types of materials, it is incapable of chemically specific identification. In contrast, s-SNIN IR mapping clearly identifies the two types of materials by their permittivities and allows further quantification of the role of thickness, composition and substrate on the IR image formation. The impressive capability of our IR s-SNIN imaging is highlighted as the thickness of the film reduces down to few atomic layers (Figure 2c and d), where the IR amplitude (A_3) contrast between the sample and the substrate is clearly superior to that of the accompanying topographic images. More importantly, these controlled samples allow us to calibrate the experimental near-field contrast and determine its correlation with the dielectric function of complex nanolayers, which depends on their chemical composition and thickness. This calibration further serves as a benchmark for the theoretical models as elaborated below.

To quantify the dielectric constants of various $In_{1-x}Ga_xN$ compositions and thicknesses based on the near-field contrast formation, we developed a theoretical approach that allows calculations of s-SNIN response on tip−sample near-field interactions. In contrast to previous models, where the effective polarizability of the tip in the presence of a sample was evaluated in semianalytical point-dipole[25] or finite-dipole approximations,[24] our novel model relies on evaluation of the tip−sample polarizability numerically using frequency-domain solver of CST Microwave Studio. Thus, we fully consider the tip−sample near-field interaction, and our model is applicable to any sample (not just thin films) without any fitting parameters. In this model, the whole conical shape of the tip illuminated by a plane electromagnetic wave is considered and the full structure of the sample including the various layers of the substrate is fully accounted for to simulate the experiment. Figure 3a shows an image example of an actual simulation of the probe tip−sample interaction. It depicts an image of the full simulation of the field strength calculated for a 10 nm-thick $In_{0.5}Ga_{0.5}N$ nanolayer on the InN substrate using frequency-domain solver of CST Microwave Studio. We then use the height-dependent reflectivity $r^{(CST)}$ (h) calculated by the CST solver to evaluate the effective tip−sample polarizability α_{eff} (h) $= ia_1a_2$ $(r^{(CST)}$ $(h))*e^{-2ik_0\cos(\theta)(z_{max}-z_{pos})}/(2\pi k_0$ $\tan$ $\theta)$. Here, a_1 and a_2 are the dimensions of the simulation box along the x- and y-axes, respectively (periodic boundary conditions are imposed), k_0 is the wave vector of the incident beam, and θ is the angle of incidence, z_{max} is the upper boundary of the simulation box, and z_{pos} is the coordinate of the substrate surface. The effective polarizability is then used to calculate the far-field radiation given by E_S $(h_0 + \Delta h \sin \omega t) = \sum_n s_n e^{in\omega_\tau t}$, where s_n is the complex s-SNIN signal, n is the demodulation order, and ω_τ is the natural frequency of the probe tip. (To simulate the experiments, we combine E_S with a reference field E_M that is reflected from an oscillating mirror, implementing a pseudoheterodyne interferometer scheme). The main simu-

DOI: 10.1021/acsami.6b06766
ACS Appl. Mater. Interfaces 2016, 8, 23160−23166

lation steps and their relation to the experimental setup are schematically shown in Figure 3a. To compare with experiment, we theoretically demodulate normalized amplitude s-SNIN signal which is extracted by dividing the signal at the sample by that at the substrate:

$$(A_{\mathrm{norm}})_n = \frac{|s_n(\mathrm{sample})|}{|s_n(\mathrm{substrate})|}$$

In Figure 3b, we show the dependence of the measured near-field normalized amplitude signal (A_3) on the sample thickness. The red line (drawn as a guide to the eye) connects the experimental dots acquired by normalizing the amplitude (A_3) signal on $In_{0.5}Ga_{0.5}N$ nanolayers to that on the InN/sapphire substrate. The normalized amplitude signal decreases as the thickness increases. Since both composition and thickness contribute to the variation in near-field amplitude signal, a decreasing amplitude (A_3) contrast with decreasing thickness implies the increasing role of the underlying substrate to the optical signal.

Using literature reports for the permittivity of Pt tip, $In_{1-x}Ga_xN$ and InN in the mid-IR spectral range, we calculated the normalized amplitude signal as a function of the nanolayer thickness. Figure 3c displays the outcome of these simulations. The theoretical plots reproduce the experimentally observed trend of decreasing amplitude signal with increasing thickness. This is expected since pure GaN ($x = 1$) has a smaller dielectric constant compared to InN. Furthermore, as the Ga content decreases ($x \rightarrow 0$), the dielectric constant of $In_{1-x}Ga_xN$ approaches that of the InN substrate, which decreases the amplitude contrast.

Using the complementary results of our novel theoretical model and the high-resolution experimental results described above on controlled patterned samples, we now address the outstanding issues regarding phase separation and composition profiles on single group III−N semiconductor QDs and complex nanoalloys. In Figure 4, we show the topography and near-field amplitude (A_2) images as well as line profiles of $In_{0.7}Ga_{0.3}N$ QDs grown on InN/sapphire templates. The topography image (Figure 4b) shows dome-shaped QDs with height ranging 5−14 nm and lateral diameter in the range 60−90 nm. The corresponding amplitude image displayed in Figure 4c shows that some of the QDS exhibit mixed optical contrast. As an example of such a mixed contrast, we selected a single particle highlighted by a yellow circle on the topography and by a black circle on the amplitude image (Figure 4b and Figure 4c, respectively) with the corresponding line profiles shown in Figure 4d and e. The selected particle is ~7 nm in height and ~70 nm in width (fwhm). In the amplitude image of this chosen particle we observe dark and bright mixed contrast, which is also experienced by some (but not all) other particles as can be seen in this image. Comparison of the smooth topographic line profile (Figure 4d) and the amplitude line profile (Figure 4e) displaying varying intensity show that the observed contrast in the amplitude image does not have a corresponding topographic origin.

As discussed above, the near-field amplitude image is sensitive to permittivity of the sample; therefore, the existence of mixed contrast on a single particle indicates the presence of two materials that phase segregated on the same QD. To identify the relative permittivity of the two materials on the QD, we performed spectroscopic imaging at several laser wavelengths and compared the spectroscopic responses with

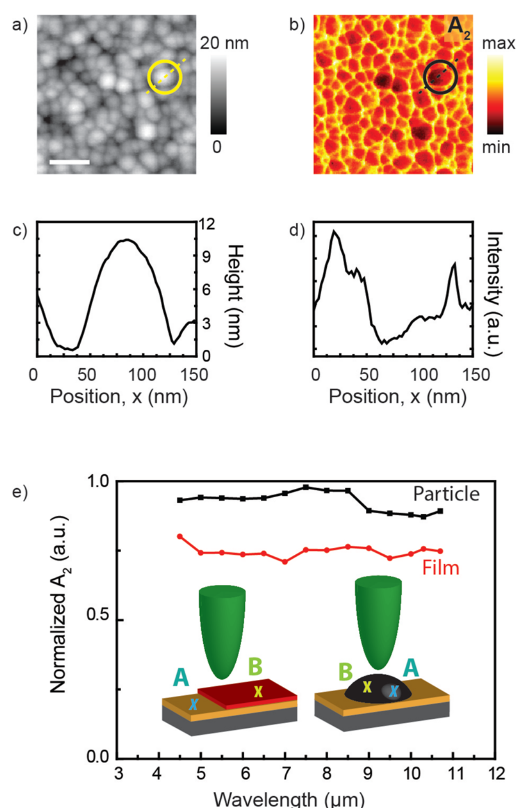

Figure 4. Experimental s-SNIN images of $In_{1-x}Ga_xN$ QDs. (a) Topography and (b) near-field amplitude (A_2) of the QDs taken at a laser wavelength of $\lambda = 10.5$ μm. (c, d) Line profiles of a selected QD of the topography and the corresponding near-field amplitude. (e) Spectroscopic plot of the experimental normalized amplitude signal of a QD (red line) and a nanolayer (black line).

that of lithographically patterned samples discussed above with similar composition and height. These experimental spectra are displayed in Figure 4e where the red points are experimental normalized amplitude values, which were obtained by taking the ratio of the signal on $In_{0.7}Ga_{0.3}N$ film to that on InN substrate (point B on the red film in the inset of Figure 4e to point A on the yellow film). The normalized amplitude values for the QD were found by dividing the signal on the dark contrast to that of the brighter contrast (point B in the nanoparticle inset in Figure 4e to that of point A). The two spectra are flat and nearly overlap in the entire wavelength region considered. From the theoretical−experimental calibration of the IR s-SNIN amplitude contrast, which we presented above on controlled patterned samples, we infer that the brighter part of the QD is an In rich region and the darker part is a Ga rich region. The normalized s-SNIN amplitude values are slightly smaller than those of the film throughout the considered spectral region. This small variation indicates that regions A and B, considered for normalization of the signal, are not pure $In_{0.7}Ga_{0.3}N$ and InN regions. Since s-SNIN can only provide a normalized (comparative) measurement, it is not possible to estimate the absolute values of dielectric functions.

To assess general statistical distribution of the phase separation, we took several near-field amplitude images at various locations of the sample. A few of these images are shown in Figure 5 These results indicate that the scale of the phase separation on a single particle varies over a wide compositional range from particle to particle ranging from

DOI: 10.1021/acsami.6b06766
ACS Appl. Mater. Interfaces 2016, 8, 23160−23166

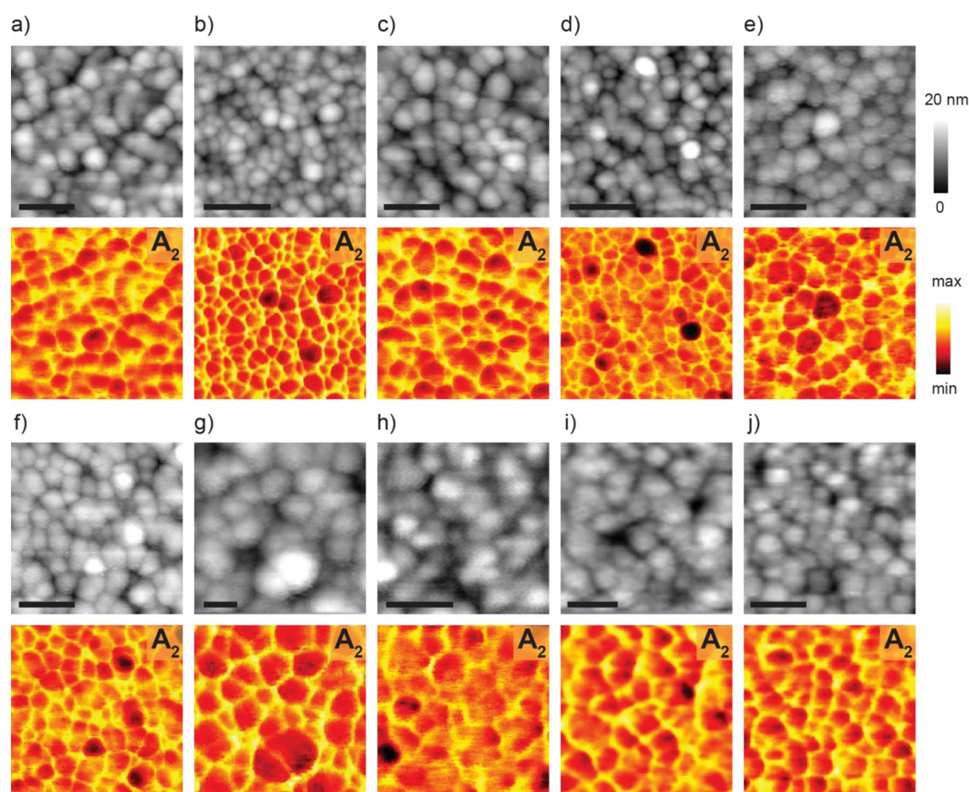

Figure 5. s-SNIN topography and near-field amplitude (A_2) images taken at several locations on the $In_{0.7}Ga_{0.3}N$ sample at a laser wavelength of λ = 10.5 μm. (a−j) Topography and accompanying 2nd harmonic near-field amplitude images taken at arbitrary locations on the sample surface. The scale bars on topographic images indicate 200 nm.

statistically Ga-rich to all In-rich QDs. An estimation of the percentage of particles that show some level of Ga-rich phase separation over the entire sample region scanned within the resolution and sensitivity of s-SNIN is between ∼20−25%. For our $In_{0.7}Ga_{0.3}N$ samples that were grown at 775 °C, this estimation is in qualitative agreement with predication based on the theoretical phase diagram of $In_{1-x}Ga_xN$ system calculated assuming a constant average value for the solid phase interaction parameter.[28] In a model used by Stringfellow et al.,[28] $In_{0.7}Ga_{0.3}N$ at a growth temperature of 775 °C is thermodynamically not stable and may segregate into stable In-rich and Ga-rich InGaN alloy regions. The probability that it could stabilize to a Ga-rich region depends on the kinetic stabilization of the growth surface, growth temperature, group V/III precursor ratio, simultaneous or sequential precursor supply, and various other processing conditions, which are presently explored by MEPA-MOCVD and verified by s-SNIN.

As described above, our theoretical model allows us to simulate the near-field coupling between the full tip and any size and shape nanoparticle as well as layers of substrate. Since our growth technique covers a wide size distribution, we investigate the dependence of the near-field tip−sample coupling on the geometry and size of the nanoparticles using our theoretical model. The simulated field distribution for two different particle sizes that are both larger than the tip apex are displayed in Figure 6a and b. The lateral size of our particles is comparable or larger than the tip apex (>60 nm diameter), so we do not expect contrast reversal to play a role.[29,30] Spectroscopic simulation using literature data for the permittivity of InGaN on InN substrate in the mid-IR wavelength region is shown in Figure 6c for large (red) and

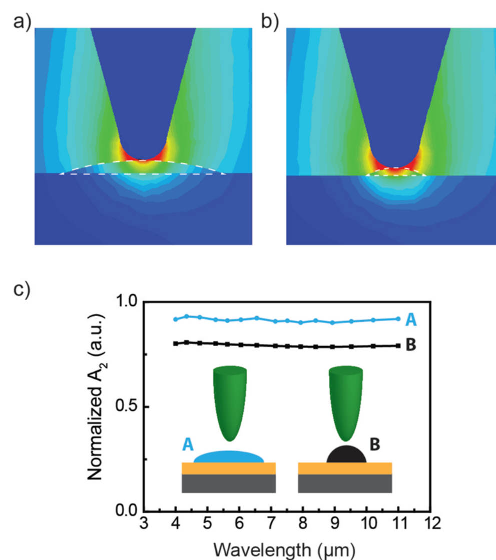

Figure 6. Numerical simulations of tip−sample interaction and spectra. (a, b) Electric field distribution of tip−sample coupling for large particle (a) and small particle (b). (c) Calculations of the spectra of near-field interaction between large and small particles.

small (black) particles. Similar to experimental results, the simulation shows a flat response across the spectral window considered. The near-field contrast (normalized amplitude signal) is larger for small particles than it is for larger particles (approximating a flat film). This is because of the competing tip−sample and tip−substrate coupling, which is a well-known size effect in s-SNIN.[29,30] For the smaller particle (Figure 6b),

DOI: 10.1021/acsami.6b06766
ACS Appl. Mater. Interfaces 2016, 8, 23160−23166

the near-field coupling with the substrate is larger compared to the near-field coupling to the particle which will render the signal on the particle weaker. Increasing the particle size (Figure 6a) strengthens the tip near-field coupling to the particle, which results in a stronger signal on the particle as clearly seen in Figure 6c. Such important size effects must be considered when analyzing the near-field response of QDs both experimentally and theoretically.

■ CONCLUSION

We have directly imaged phase segregation at a nanometer spatial scale in epitaxial $In_{1-x}Ga_xN$ alloys using high-resolution s-SNIN. Using a combination of plasma-assisted CVD and lithographically structured InN/sapphire templates with subsequent deposition of $In_{1-x}Ga_xN$ nanolayers, we calibrated the s-SNIN near-field contrast of $In_{1-x}Ga_xN$ between GaN and InN. In s-SNIN the amplitude signal contrast depends on the local dielectric constant of the sample below the probe tip. The normalized signal contrast is determined by taking the ratio of the signal on the sample to that on the substrate. To guide the experiments in quantifying the near-field contrast and, subsequently, the dielectric constants of $In_{1-x}Ga_xN$ alloys, we have developed an advanced s-SNIN model that fully describes the near-field coupling between the probe tip, the sample, and the substrate. In comparison to previous models, where the effective polarizability of the tip in the presence of a thin film was evaluated semianalytically in the point-dipole or finite-dipole approximations, our model is more accurate, and it is applicable to samples with a complex geometry. We evaluate the tip−sample polarizability numerically considering the conical shape of the tip and the entire tip−sample near-field interaction accounting for the full structure of the sample layers. The results presented in this work, as well as our experimental and theoretical techniques, present a significant step forward toward clarifying and quantifying the nanoscale phase segregation of indium and gallium in the $In_{1-x}Ga_xN$ lattice, which is a crucial step toward understanding fundamental kinetic processes leading to the nanoscale phase segregation at the growth surface. This allows us to tailor the growth surface chemistry to either avoid the segregation process or engineer it to obtain new device functionalities as well as improved optical devices with increased internal device efficiency.

■ METHODS

Group III−N epilayers, heterostructures and nanostructured alloys were grown in a customized migration-enhanced plasma-assisted metal organic chemical vapor deposition (MEPA-MOCVD) reactor. The epitaxial deposition process for InGaN alloys was carried out with precursors supplied mode, varying plasma and MO exposures, precursor separation times, reactor pressure, and growth temperature.[2] A set of InN epilayers were deposited and masked with a two-dimensional (2D) pattern of silicon dioxide (SiO_2) columns by holographic lithography.[3] The patterned InN/sapphire templates were overgrown with GaN or different $In_{1-x}Ga_xN$ compositions during simultaneous MO supply by MEPA-MOCVD. After the overgrowth, the SiO_2 mask was removed, exposing the underlying InN/sapphire template and acting as a base reference for the deposited GaN and $In_{1-x}Ga_xN$ nanolayers. The patterned $In_{1-x}Ga_xN$ nanolayers of various compositions and thickness were used to calibrate the s-SNIN IR contrast.

■ AUTHOR INFORMATION

Corresponding Author

*E-mail: yabate@gsu.edu.

Notes

The authors declare no competing financial interest.

■ ACKNOWLEDGMENTS

Y.A. and A.F. acknowledge support for this work from the Air Force Office of Scientific Research (AFOSR) grant number FA9559-16-1-0172. S.G. acknowledges support provided by National Science Foundation grant no. 1553251. N.D. acknowledges support by AFOSR award no. FA9550-10-1-0097. M.I.S. gratefully acknowledges major support of a grant no. DE-SC0007043 from the Office of Basic Energy Sciences, Office of Science, the U.S. Department of Energy. Research of V.S.Y. was supported by a MURI grant no. N00014-13-1-0649 from the U.S. Office of Naval Research, the U.S. Department of Defense. Support of V.B. came from a grant no. DE-FG02-01ER15213 from the Office of Basic Energy Sciences, Office of Science, the U.S. Department of Energy.

■ REFERENCES

(1) Akasaki, I.; Amano, H. Breakthroughs in Improving Crystal Quality of GaN and Invention of the P-N Junction Blue-Light-Emitting Diode. *Jpn. J. Appl. Phys., Part 1* **2006**, *45*, 9001−9010.

(2) Kojima, K.; Funato, M.; Kawakami, Y.; Nagahama, S.; Mukai, T.; Braun, H.; Schwarz, U. T. Gain Suppression Phenomena Observed in $In_xGa_{1-x}N$ Quantum Well Laser Diodes Emitting at 470 nm. *Appl. Phys. Lett.* **2006**, *89*, 241127.

(3) Nagahama, S.; Yanamoto, T.; Sano, M.; Mukai, T. Characteristics of InGaN Laser Diodes in the Pure Blue Region. *Appl. Phys. Lett.* **2001**, *79*, 1948−1950.

(4) Nakamura, S. The Roles of Structural Imperfections in InGaN-Based Blue Light-Emitting Diodes and Laser Diodes. *Science* **1998**, *281*, 956−961.

(5) Tran, C. A.; Karlicek, R. F.; Schurman, M.; Osinsky, A.; Merai, V.; Li, Y.; Eliashevich, I.; Brown, M. G.; Nering, J.; Ferguson, I.; Stall, R. Phase Separation in InGaN/GaN Multiple Quantum Wells and its Relation to Brightness of Blue and Green LEDs. *J. Cryst. Growth* **1998**, *195*, 397−400.

(6) Zhu, D.; Wallis, D. J.; Humphreys, C. J. Prospects of III-Nitride Optoelectronics Grown on Si. *Rep. Prog. Phys.* **2013**, *76*, 106501−106501.

(7) Bormann, I.; Brunner, K.; Hackenbuchner, S.; Zandler, G.; Abstreiter, G.; Schmult, S.; Wegscheider, W. Midinfrared Intersubband Electroluminescence of Si/SiGe Quantum Cascade Structures. *Appl. Phys. Lett.* **2002**, *80*, 2260−2262.

(8) Grandjean, N.; Massies, J.; Dalmasso, S.; Vennegues, P.; Siozade, L.; Hirsch, L. GaInN Gan Multiple-Quantum-Well Light-Emitting Diodes Grown by Molecular Beam Epitaxy. *Appl. Phys. Lett.* **1999**, *74*, 3616−3618.

(9) Ludwig, C. D. R.; Gruhn, T.; Felser, C.; Schilling, T.; Windeln, J.; Kratzer, P. Indium-Gallium Segregation in $CuIn_xGa_{1-x}Se_2$: An ab Initio-Based Monte Carlo Study. *Phys. Rev. Lett.* **2010**, *105*, 025702.

(10) Muraki, K.; Fukatsu, S.; Shiraki, Y.; Ito, R. Surface Segregation of In Atoms and its Influence on the Quantized Levels in InGaAs/GaAs Quantum-Wells. *J. Cryst. Growth* **1993**, *127*, 546−549.

(11) Chattopadhyay, K.; Aubel, J.; Sundaram, S.; Ehret, J. E.; Kaspi, R.; Evans, K. R. Electroreflectance Study of Effects of Indium Segregation in Molecular-Beam-Epitaxy-Grown InGaAs/GaAs. *J. Appl. Phys.* **1997**, *81*, 3601−3606.

(12) Cho, J. H.; Zhang, S. B.; Zunger, A. Indium-Indium Pair Correlation and Surface Segregation in InGaAs Alloys. *Phys. Rev. Lett.* **2000**, *84*, 3654−3657.

(13) Duxbury, N.; Bangert, U.; Dawson, P.; Thrush, E. J.; Van der Stricht, W.; Jacobs, K.; Moerman, I. Indium Segregation in InGaN Quantum-Well Structures. *Appl. Phys. Lett.* **2000**, *76*, 1600−1602.

(14) Gerard, J. M.; D'Anterroches, C. Growth Of InGaAs/GaAs Heterostructures with Abrupt Interfaces on the Monolayer Scale. *J. Cryst. Growth* **1995**, *150*, 467−472.

DOI: 10.1021/acsami.6b06766
ACS Appl. Mater. Interfaces 2016, 8, 23160−23166

(15) Litvinov, D.; Gerthsen, D.; Rosenauer, A.; Schowalter, M.; Passow, T.; Feinaeugle, P.; Hetterich, M. Transmission Electron Microscopy Investigation of Segregation and Critical Floating-Layer Content of Indium for Island Formation in $In_xGa_{1-x}As$. *Phys. Rev. B: Condens. Matter Mater. Phys.* **2006**, *74*, 165306.
(16) Muraki, K.; Fukatsu, S.; Shiraki, Y.; Ito, R. Surface Segregation of in Atoms During Molecular-Beam Epitaxy and its Influence on the Energy-Levels in InGaAs/GaAs Quantum-Wells. *Appl. Phys. Lett.* **1992**, *61*, 557−559.
(17) Sato, M.; Horikoshi, Y. Effect of Indium Replacement by Gallium on InAs/GaAs Quantized Levels. *Surf. Sci.* **1992**, *267*, 195−198.
(18) Jinschek, J. R.; Kisielowski, C. Time, Energy, and Spatially Resolved TEM Investigations of Defects in InGaN. *Phys. B* **2006**, *376-377*, 536−539.
(19) Feng, Z. C.; Liu, W.; Chua, S. J.; Yu, J. W.; Yang, C. C.; Yang, T. R.; Zhao, J. Photoluminescence Characteristics of Low Indium Composition InGaN Thin Films Grown on Sapphire by Metalorganic Chemical Vapor Deposition. *Thin Solid Films* **2006**, *498*, 118−122.
(20) Davis, R. F.; Roskowski, A. M.; Preble, E. A.; Speck, J. S.; Heying, B.; Freitas, J. A.; Glaser, E. R.; Carlos, W. E. Gallium Nitride Materials - Progress, Status, and Potential Roadblocks. *Proc. IEEE* **2002**, *90*, 993−1005.
(21) Ozturk, M. K.; Corekci, S.; Tamer, M.; Cetin, S. S.; Ozcelik, S.; Ozbay, E. Microstructural Properties of InGaN/GaN Light-Emitting Diode Structures with Different In Content Grown by MOCVD. *Appl. Phys. A: Mater. Sci. Process.* **2014**, *114*, 1215−1221.
(22) Keilmann, F.; Hillenbrand, R. Near-Field Microscopy by Elastic Light Scattering from a Tip. *Philos. Trans. R. Soc., A* **2004**, *362*, 787−805.
(23) Hillenbrand, R.; Keilmann, F. Complex Optical Constants on a Subwavelength Scale. *Phys. Rev. Lett.* **2000**, *85*, 3029−3032.
(24) Stiegler, J. M.; Abate, Y.; Cvitkovic, A.; Romanyuk, Y. E.; Huber, A. J.; Leone, S. R.; Hillenbrand, R. Nanoscale Infrared Absorption Spectroscopy of Individual Nanoparticles Enabled by Scattering-Type Near-Field Microscopy. *ACS Nano* **2011**, *5*, 6494−6499.
(25) Knoll, B.; Keilmann, F. Enhanced Dielectric Contrast in Scattering-Type Scanning Near-Field Optical Microscopy. *Opt. Commun.* **2000**, *182*, 321−328.
(26) Hillenbrand, R.; Keilmann, F. Material-Specific Mapping of Metal/Semiconductor/Dielectric Nanosystems at 10 nm Resolution by Backscattering Near-Field Optical Microscopy. *Appl. Phys. Lett.* **2002**, *80*, 25−27.
(27) Abate, Y.; Ziegler, J.; Gamage, S.; Javani, M. H.; Stockman, M. I.; Haglund, R. F.; et al. Control of Plasmonic Nanoantennas by Reversible Metal-Insulator Transition. *Sci. Rep.* **2015**, *5*, 13997−13997.
(28) Ho, I. H.; Stringfellow, G. B. Solid Phase Immiscibility in GaInN. *Appl. Phys. Lett.* **1996**, *69*, 2701−2703.
(29) Kim, Z. H.; Ahn, S.-H.; Liu, B.; Leone, S. R. Nanometer-Scale Dielectric Imaging of Semiconductor Nanoparticles: Size-Dependent Dipolar Coupling and Contrast Reversal. *Nano Lett.* **2007**, *7*, 2258−2262.
(30) Abate, Y.; Schwartzberg, A.; Strasser, D.; Leone, S. R. Nanometer-Scale Size Dependent Imaging of Cetyl Trimethyl Ammonium Bromide (CTAB) Capped and Uncapped Gold Nanoparticles by Apertureless Near-Field Optical Microscopy. *Chem. Phys. Lett.* **2009**, *474*, 146−152.
(31) Giugni, A.; Torre, B.; Toma, A.; Francardi, M.; Malerba, M.; Alabastri, A.; Proietti Zaccaria, R.; Stockman, M. I.; Di Fabrizio, E. Hot-Electron Nanoscopy Using Adiabatic Compression of Surface Plasmons. *Nat. Nanotechnol.* **2013**, *8*, 845−852.

DOI: 10.1021/acsami.6b06766
ACS Appl. Mater. Interfaces 2016, 8, 23160−23166